The Hydrodynamic Behavior of Vortex Shedding behind Circular Cylinder in the Presence of Group Focused Waves

Iskander Abroug, Nizar Abcha, Fahd Mejri, Emma Imen Turki, Elena Ojeda

fluids

MDPI

Article

The Hydrodynamic Behavior of Vortex Shedding behind Circular Cylinder in the Presence of Group Focused Waves

Iskander Abroug, Nizar Abcha *, Fahd Mejri, Emma Turki and Elena Ojeda

Normandie Université, UNICAEN, UNIROUEN, CNRS, UMR 6143 M2C, 14000 Caen, France; iskander.abroug@unicaen.fr (I.A.); fahdmejri93@gmail.fr (F.M.); imen.turki@univ-rouen.fr (E.T.); eleojeda@gmail.com (E.O.)

* Correspondence: nizar.abcha@unicaen.fr

Abstract: Vortex shedding behind an elastically mounted circular cylinder in the presence of group focused waves propagating upstream was investigated using a classical approach (time series and FFT) and nonclassical approach (complex 2D Morlet wavelets). Wavelet analysis emerged as a novel solution in this regard. Our results include wave trains with different nonlinearities propagating in different water depths and derived from three types of spectra (Pierson–Moskowitz, JONSWAP (γ = 3.3 or γ = 7)). It was found that the generated wave trains could modify regimes of shedding behind the cylinder, and subharmonic frequency lock-in could arise in particular situations. The occurrence of a lock-in regime in the case of wave trains propagating in intermediate water locations was shown experimentally even for small nonlinearities. Moreover, the application of time-localized wavelet analysis was found to be a powerful approach. In fact, the frequency lock-in regime and its duration could be readily identified from the wavelet-based energy and its corresponding ridges.

Keywords: vortex shedding; subharmonic synchronization; circular cylinder; group focused waves; JONSWAP; Pierson–Moskowitz; wavelet analysis; ridges

Citation: Abroug, I.; Abcha, N.; Mejri, F.; Turki, E.; Ojeda, E. The Hydrodynamic Behavior of Vortex Shedding behind Circular Cylinder in the Presence of Group Focused Waves. *Fluids* **2022**, *7*, 4. https://doi.org/10.3390/fluids7010004

Academic Editor: Mehrdad Massoudi

Received: 10 November 2021
Accepted: 20 December 2021
Published: 22 December 2021

1. Introduction

Vortex shedding behind cylindrical structures has been the focus of many experimental and numerical studies over recent decades, given its practical importance in the maritime industry [1–4]. When exposed to highly nonlinear perturbations, vortex shedding provides modifications particularly in the wake around the cylinder. Therefore, these modifications should be considered when evaluating vortex shedding's disadvantages. The frequency of vortex shedding f_{sh} in the wake depends on the frequency of the perturbation f_w. More precisely, there is a fundamental synchronization region in which f_{sh} is controlled by the imposed perturbation, which is referred to as the vortex shedding lock-in regime [5,6]. This regime may occur at frequencies of perturbation f_w equal to f_{sh} (harmonic lock-in), $2f_{sh}$ (subharmonic lock-in), or f_{sh}/n with $n = 2, 3, \ldots$ (superharmonic lock-in) [7]. In the present work, we only focused on subharmonic lock-in regime, i.e., $f_w \sim 2f_{sh}$.

In the global context of climate change evolving the expansion of marine renewable energy and the impacts of storminess on man-induced frames, cylindrical structures should be designed to remain functional in increasingly intermediate and deep-water locations during extreme events. For that reason, it is essential to study vortex shedding around the cylinder in similar harsh environments. In previous studies, several physical mechanisms have been suggested as causing the formation of extreme waves, including dispersive focusing in shallow or intermediate water depth [8,9] and modulation instability in deep-water depth, i.e., $kh > 1.363$, where k and h are the wavenumber and water depth, respectively [10]. In the present work, we have decided to limit our focus to extreme waves generated by the spatiotemporal wave focusing as a consequence of the dispersive nature of water waves. Dispersive focusing is traditionally used in laboratory modeling [11–13] to represent the expected wave profile based on the NewWave theory [14], which describes the wave velocity components and the free surface elevation of a focused group of localized waves. The

waves are superposed and brought into phase at one point, generating an extreme wave event. The impact of wave trains on the structure of vortices behind the cylinder has not yet been investigated. Therefore, we will study the features of frequency lock-in of vortex shedding in the wake when the external forcing is due to wave trains.

The most widely used frequency analysis technique to detect the shedding frequency in the wake of a cylinder is the Fast Fourier Transform (FFT) [7]. Given the rapidly changing nature of extreme waves, the reliability of the forecast of extreme waves' impact on the wake behind the cylinder using FFT is low and hard to temporally expect. Consequently, FFT does not reflect the accurate time localization of the subharmonic frequency lock-in. In this work, we explore the capabilities of the complex wavelet convolution tool to improve the localization of the subharmonic lock-in. The need to evaluate relatively long-term and highly random phenomena using wavelet analysis is already found in a variety of disciplines, such as plasma physics [15], health-related areas like neuroscience [16], geophysics [17], or ocean wave analysis [18–20].

Observations of the shedding frequency f_{sh} in the wake of an elastically mounted cylinder subjected to wave trains are presented in this paper. Firstly, a spectral analysis was used in order to investigate the spectral changes in the wake of the cylinder from random wave trains with a wide range of water depth, nonlinearities, and spectra types. Secondly, wavelet analysis was proposed as a tool to identify the temporal evolution of subharmonic frequency lock-in based on the wavelet transform.

The remainder of this paper is organized as follows. Section 2 describes our experimental set-up. Section 3 is devoted to our experimental results and observations. The fourth and last sections present our conclusions and perspectives.

2. Materials and Methods

The tests were conducted at the Morphodynamique Continentale et Côtière de Caen, France. The wave flume was 16 m long, 0.5 m wide, and filled with tap water to a depth of h_0 = 0.25 m (Figure 1). A piston-type wave maker was located at one end of the flume to generate wave trains, and a foam absorber beach was at the other end. Two honeycombs of about 20 cm were installed in the flume, as shown in Figure 1a, in order to reduce wave reflection and to minimize the intensity of turbulent fluctuations generated by the pump. Temporal variations of free surface elevation measured at x = 2 m from the wave maker, were recorded by a wave gauge with a sampling rate of 100 Hz. These measurements were used to identify input wave train parameters.

The experimental setup is shown in Figure 1. The rigid circular cylinder model, situated at x = 7 m from the wave maker, was made from Plexiglas with diameter D = 0.04 m and had an immersed length of L = 0.248 m. An acoustic doppler velocimeter (ADV), placed at a distance $d \sim$ D from the cylinder, was used to measure the longitudinal wave velocity V_x upstream the structure. Wave trains propagated on the background of a steady current U = 0.16 m/s, corresponding to a Reynolds number $Re = \frac{UD}{\nu} = 6400$ (ν is the kinematic viscosity) and a Froude number $Fr = \frac{U}{\sqrt{gh_0}} = 0.1$. The definition of the flow velocity and the Reynolds and Froude numbers were the same as in Hans et al. (2016). The cylinder was vertically clamped by its upper end to an elastic support, which was fixed on the flume's structure. The lower end of the cylinder was at approximately 2 mm (5% D) from the flume's floor (Figure 1b,c).

Focused wave trains were generated with a technique similar to that in [13]. The resulting wave trains were derived from Pierson–Moskowitz, JONSWAP (γ = 3.3), and JONSWAP (γ = 7) spectra. Figure 2 shows three sets of time series of Pierson–Moskowitz, JONSWAP (γ = 3.3), and JONSWAP (γ = 7) wave trains and their corresponding dimensionless frequency spectra.

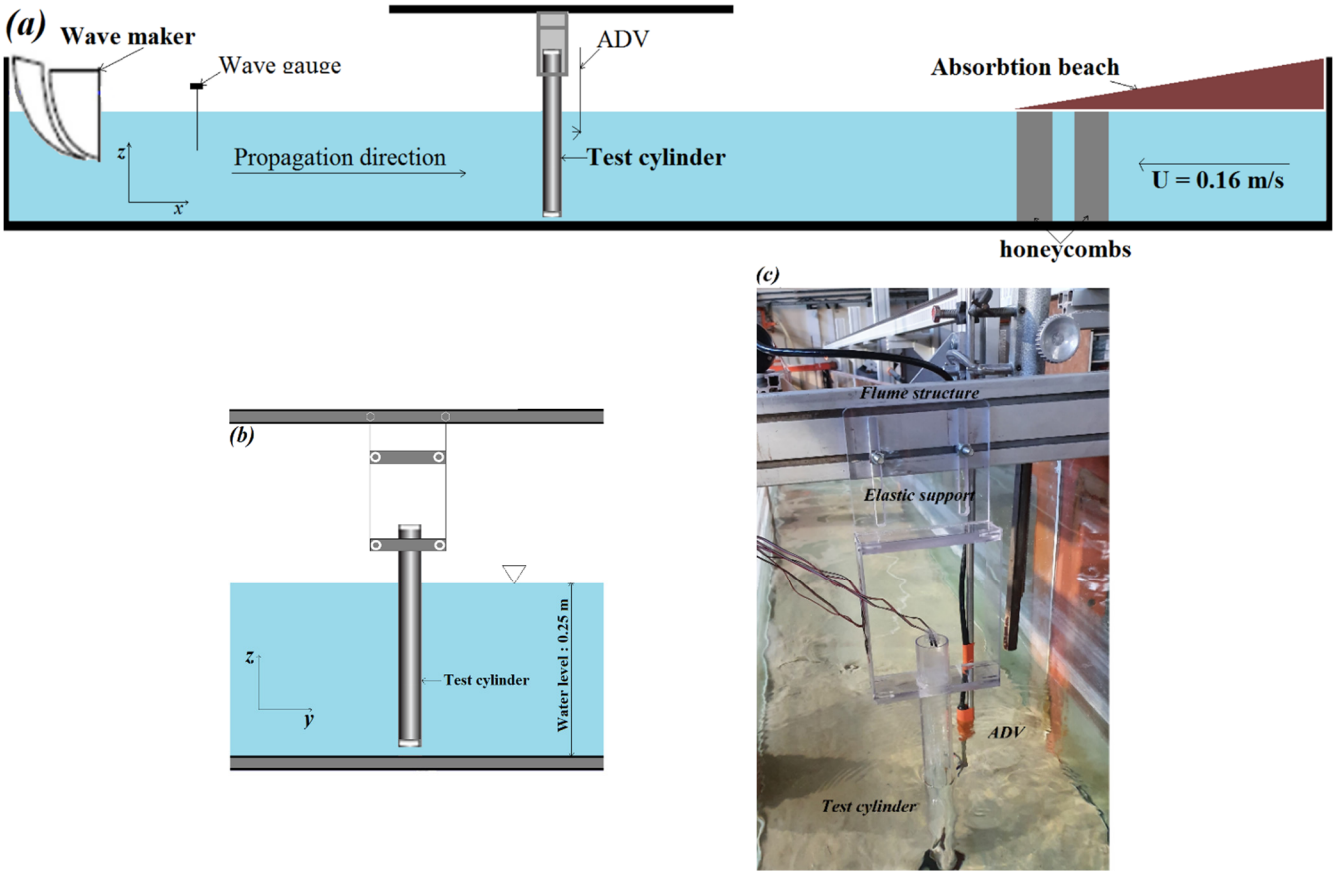

Figure 1. A schematic showing the experimental setup in the test section of the water flume: (**a**) longitudinal view; (**b**) cross section view; (**c**) photo of the cylinder and the elastic base mounted on the flume structure.

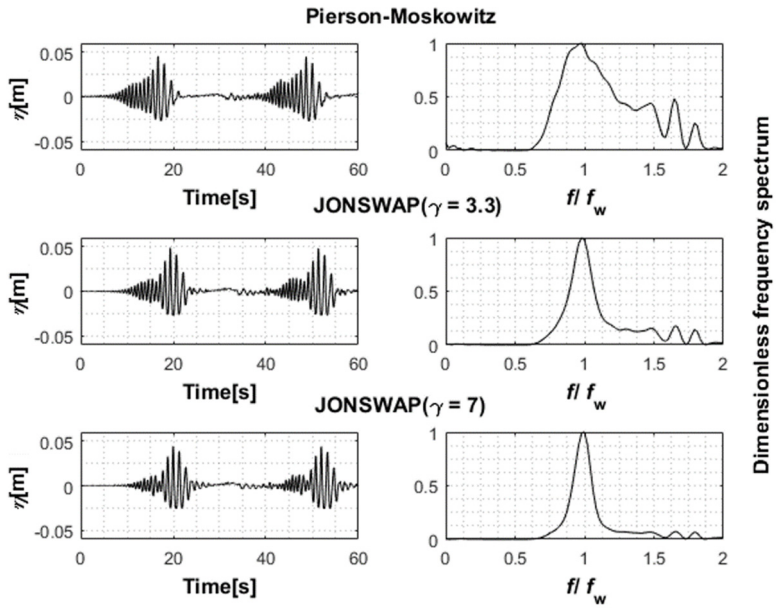

Figure 2. Three sets of time series of Pierson–Moskowitz (Case 10), JONSWAP (γ = 3.3) (Case 48), JONSWAP (γ = 7) (Case 86) wave trains and their corresponding dimensionless frequency spectra.

By adjusting the nonlinearity S_0, breaking wave trains with different amplitudes were generated. The focus point was set to x = 12 m > x = 7 m and therefore, all of the generated

wave trains broke downstream the cylinder. The nonlinearity parameter $S_0 = k_{S_0} \sum_{i=1}^{n} a_i$, also called local wave steepness, was the same as S_0 in [13]. Here, k_{S_0} was the characteristic wavenumber, and a_i was the amplitude of the ith wave component. The nonlinearity parameter S_0 was calculated at x = 2 m from the wave maker. The generated wave trains propagated in intermediate water depth ($0.9 < k_w h_0 < 2.04$). Tables 1 to 3 present some key parameters of the generated wave trains, which were categorized via their spectra, wave nonlinearity S_0, and the water depth $k_w h_0$. One hundred and twenty crest-focused wave groups were generated in this study.

Table 1. Summary of the primary Pierson–Moskowitz wave train parameters. f_w: peak wave frequency; k_w: wave number; S_0: wave train nonlinearity.

	f_w (Hz)	$k_w h_0$	S_0		f_w (H)	$k_w h_0$	S_0
Case 1	0.8	0.9	0.005	Case 11	1	1.2	0.001
Case 2		0.9	0.021	Case 12		1.2	0.005
Case 3		0.9	0.050	Case 13		1.2	0.012
Case 4		0.9	0.081	Case 14		1.2	0.021
Case 5		0.9	0.125	Case 15		1.2	0.034
Case 6		0.9	0.180	Case 16		1.2	0.050
Case 7		0.9	0.240	Case 17		1.2	0.067
Case 8		0.9	0.310	Case 18		1.2	0.088
Case 9		0.9	0.390	Case 19		1.2	0.110
Case 10		0.9	0.480	Case 20		1.2	0.140
	f_w (Hz)	$k_w h_0$	S_0		f_w (H)	$k_w h_0$	S_0
Case 21	1.2	1.58	0.001	Case 31	1.4	2.04	0.001
Case 22		1.58	0.001	Case 32		2.04	0.001
Case 23		1.58	0.003	Case 33		2.04	0.001
Case 24		1.58	0.006	Case 34		2.04	0.001
Case 25		1.58	0.009	Case 35		2.04	0.002
Case 26		1.58	0.014	Case 36		2.04	0.004
Case 27		1.58	0.019	Case 37		2.04	0.005
Case 28		1.58	0.026	Case 38		2.04	0.007
Case 29		1.58	0.032	Case 39		2.04	0.009
Case 30		1.58	0.040	Case 40		2.04	0.012

Table 2. Summary of the primary JONSWP (γ = 3.3) wave parameters. f_w: peak wave frequency; k_w: wave number; S_0: wave train nonlinearity.

	f_w (Hz)	$k_w h_0$	S_0		f_w (H)	$k_w h_0$	S_0
Case 41	0.8	0.9	0.010	Case 51	1	1.2	0.002
Case 42		0.9	0.036	Case 52		1.2	0.011
Case 43		0.9	0.080	Case 53		1.2	0.024
Case 44		0.9	0.140	Case 54		1.2	0.041
Case 45		0.9	0.220	Case 55		1.2	0.065
Case 46		0.9	0.313	Case 56		1.2	0.093
Case 47		0.9	0.412	Case 57		1.2	0.124
Case 48		0.9	0.514	Case 58		1.2	0.159
Case 49		0.9	0.624	Case 59		1.2	0.199
Case 50		0.9	0.734	Case 60		1.2	0.244

Table 2. *Cont.*

	f_w (Hz)	$k_w h_0$	S_0		f_w (H)	$k_w h_0$	S_0
Case 61	1.2	1.58	0.001	Case 71	1.4	2.04	0.001
Case 62		1.58	0.003	Case 72		2.04	0.001
Case 63		1.58	0.008	Case 73		2.04	0.001
Case 64		1.58	0.013	Case 74		2.04	0.002
Case 65		1.58	0.020	Case 75		2.04	0.003
Case 66		1.58	0.030	Case 76		2.04	0.004
Case 67		1.58	0.041	Case 77		2.04	0.006
Case 68		1.58	0.054	Case 78		2.04	0.008
Case 69		1.58	0.070	Case 79		2.04	0.010
Case 70		1.58	0.088	Case 80		2.04	0.012

Table 3. Summary of the primary JONSWP ($\gamma = 7$) wave parameters. f_w: peak wave frequency; k_w: wave number; S_0: wave train nonlinearity.

	f_w (Hz)	$k_w h_0$	S_0		f_w (Hz)	$k_w h_0$	S_0
Case 81	0.8	0.9	0.014	Case 91	1	1.2	0.003
Case 82		0.9	0.058	Case 92		1.2	0.014
Case 83		0.9	0.125	Case 93		1.2	0.035
Case 84		0.9	0.218	Case 94		1.2	0.066
Case 85		0.9	0.332	Case 95		1.2	0.102
Case 86		0.9	0.457	Case 96		1.2	0.144
Case 87		0.9	0.584	Case 97		1.2	0.191
Case 88		0.9	0.715	Case 98		1.2	0.247
Case 89		0.9	0.853	Case 99		1.2	0.312
Case 90		0.9	0.944	Case 100		1.2	0.381
	f_w (Hz)	$k_w h_0$	S_0		f_w (Hz)	$k_w h_0$	S_0
Case 101	1.2	1.58	0.001	Case 111	1.4	2.04	0.001
Case 102		1.58	0.005	Case 112		2.04	0.001
Case 103		1.58	0.011	Case 113		2.04	0.002
Case 104		1.58	0.020	Case 114		2.04	0.004
Case 105		1.58	0.034	Case 115		2.04	0.006
Case 106		1.58	0.053	Case 116		2.04	0.008
Case 107		1.58	0.073	Case 117		2.04	0.011
Case 108		1.58	0.096	Case 118		2.04	0.015
Case 109		1.58	0.120	Case 119		2.04	0.018
Case 110		1.58	0.144	Case 120		2.04	0.022

3. Results and Discussions

3.1. Fourier Analysis

The longitudinal velocity V_x measured downstream the cylinder and FFT analysis were used in order to obtain the velocity energy spectrum $S\ (V_x(t)) = 2\ |F(V_x(t))|^2$. Here, F was the Fourier transform of the flow velocity V_x. The sampling time for ADV measurements was truncated to 187.5 s, corresponding to 37,500 points. The lower and the upper cut-off frequencies were set, respectively, to 0.5 Hz and $2f_w$. Outside this frequency range, the spectral energy was very low (less than 2% of the total energy) and could be neglected.

Figure 3 exhibits a typical set of velocity spectra for twelve wave trains having approximately the same nonlinearity S_0, derived from the three spectra and propagating in four different water depths. For each spectrum, the amplitude was normalized by the maximum of the spectral energy, and the shedding frequency f_{sh} was normalized by the wave train peak frequency f_w. The ratio f_{sh}/f_w and the spectrum width were used as indicators for detecting the subharmonic synchronization regime. In Hans et al. (2016), a spectral width of less than 3% of $f_{sh}/f_w = 0.5$ was used, in the case of regular waves, as a criterion by which

it is possible to know if the frequency lock-in occurred or not. In this study, the presence of a subharmonic-like regime was characterized by $f_{sh}/f_w = 0.5$ and a spectrum width $\Delta f = 10\%$ of $f_{sh}/f_w = 0.5$, in which more than 90% of the total energy was present.

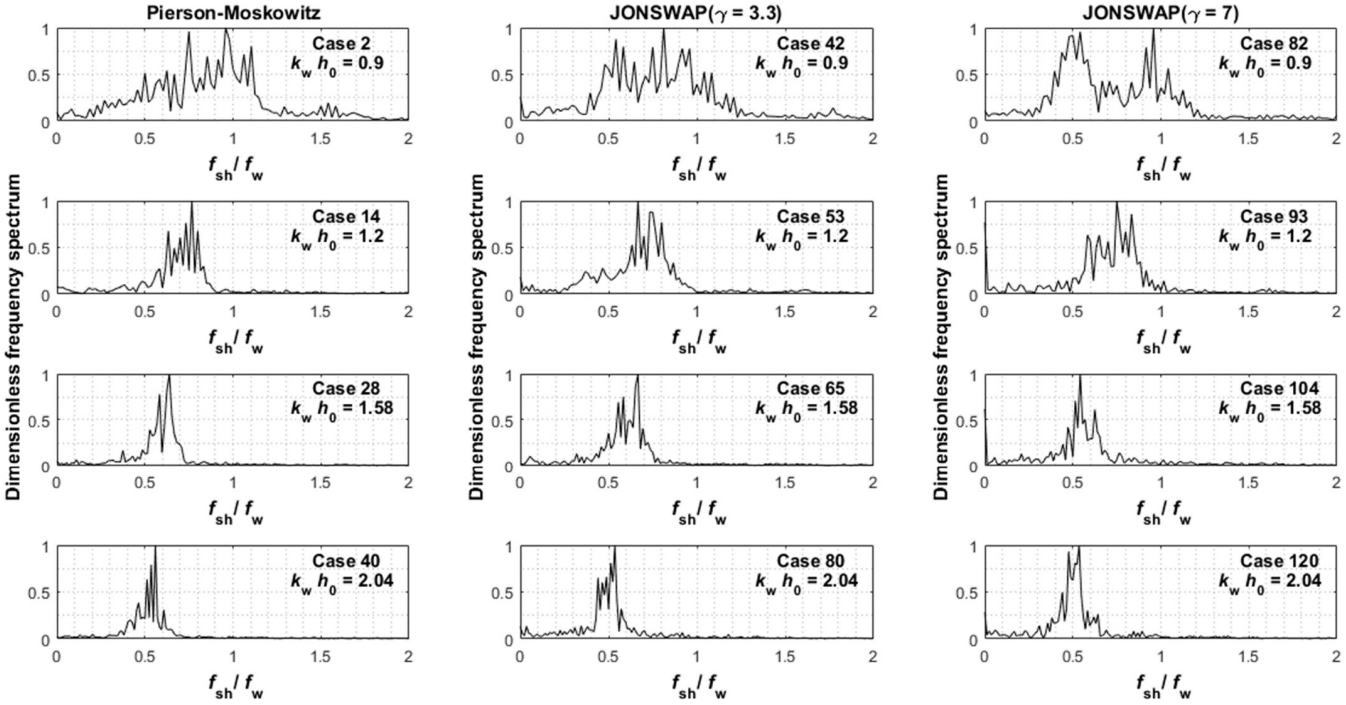

Figure 3. Velocity spectra of twelve wave trains having approximately the same nonlinearity S_0 with varying the water depth $k_w h_0$.

As the water depth increased, decreasing shedding frequency was featured, and the energy accumulation near $f = f_w/2$ was evident. The existence of the subharmonic-like regime narrowed the high and low amplitude range of the velocity spectra. The shedding frequency and the wave peak frequency subsynchronized at $k_w h_0 > 2.04$, while the FFT spectra of the ADV signal were broad-banded with peak frequencies higher than $f_{sh}/f_w = 0.5$ in shallower water depths $k_w h_0 < 2.04$.

The dominant frequency of longitudinal velocity fluctuations in the wake f_{sh} measured for all the studied wave trains is summarized in Figure 4. One can observe that the wave nonlinearity S_0 and the spectrum type had no noticeable impact on the behavior of the shedding frequency evolution versus the steepness.

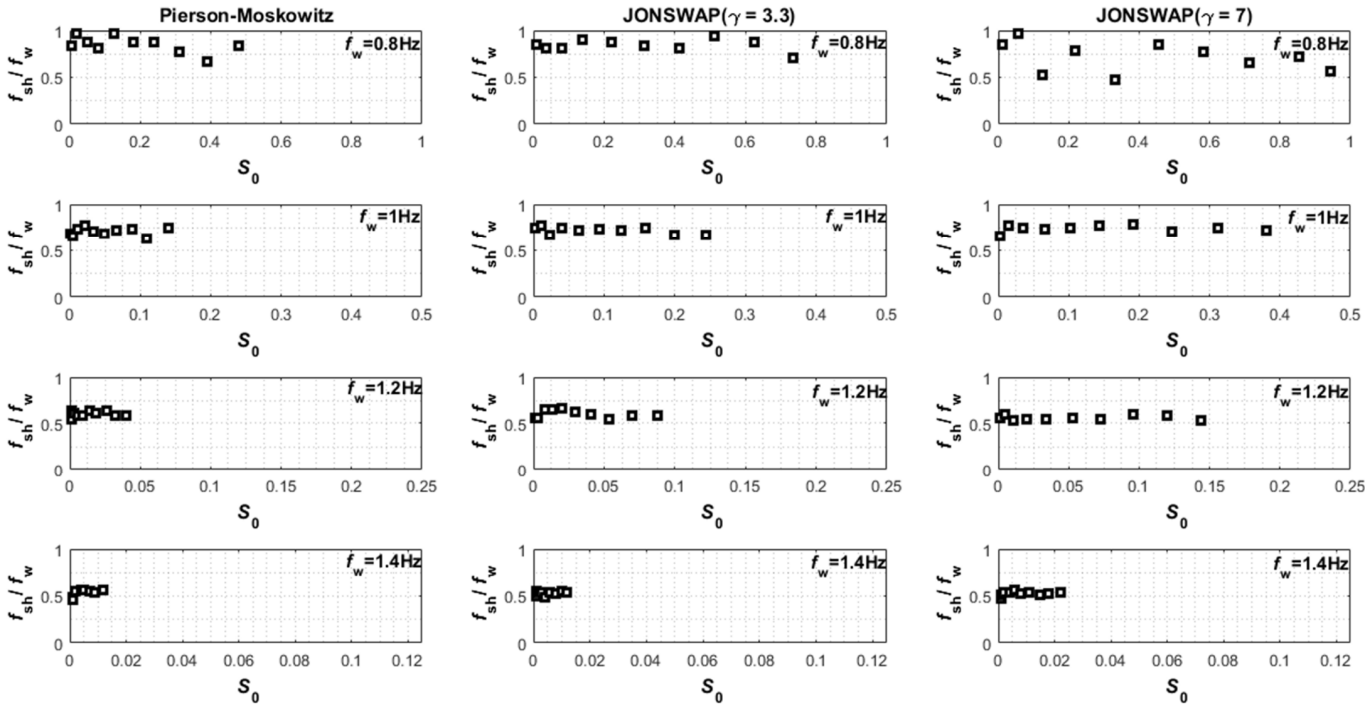

Figure 4. The evolution of the normalized shedding frequency f_{sh}/f_w relative to wave nonlinearity S_0.

3.2. Wavelet Analysis

The spectral method used in the last section did not take into account signals whose constituent frequencies varied over time. Consequently, we needed a tool that has high resolution in the frequency and time domain, allowing us to identify at which frequencies the signal oscillated, and most importantly, at which time they occurred [21]. To efficiently and accurately detect frequency lock-in in the wake of the cylinder, the wavelet transform was proposed. Among all tests, the experimental results of six representative cases are provided in Table 4. It is important to note that similar results were obtained for the remaining wave trains.

Table 4. Selected wave trains; JS: JONSWAP and PM: Pierson–Moskowitz.

Cases	*Spectrum*	f_w	$k_w h_0$	S_0	*Lock-In*
2	PM	0.8	0.9	0.021	Absence
35	PM	1.4	2.04	0.002	Presence
46	JS (3.3)	0.8	0.9	0.313	Absence
72	JS (3.3)	1.4	2.04	0.001	Presence
90	JS (7)	0.8	0.9	0.944	Absence
111	JS (7)	1.4	2.04	0.001	Presence

The continuous wavelet transform $WT\ (a,\tau)$ of the ADV temporal signal $V_x\ (t)$ was defined as a convolution integral of $V_x\ (t)$ with dilated and scaled versions of a so-called mother wavelet $\psi^*_{a,\tau}$ [22,23]:

$$WT\ (a,\tau) = \int_{-\infty}^{+\infty} V_x\ (t)\ \psi^*_{a,\tau}\ dt \quad (1)$$

The asterisk indicates the complex conjugate, and $\psi_{a,\tau}$ represents the so-called mother wavelet function dilated by a factor τ and scaled by a factor a. Informally, $V_x(t) \times \psi_{a,\tau}$

represents the energy of the ADV temporal signal around time t in the frequency band centered at 2^i. Hence, scales can be written as fractional powers of two [23]:

$$a_i = a_0 2^{i\delta},\ i = 1, 2, 3 \ldots M \tag{2}$$

$$M = \frac{1}{\delta} log_2 \left(\frac{N\Delta t}{a_0} \right) \tag{3}$$

where a_0 = 0.01 is the smallest resolvable scale, M denotes the largest scale, and δ is the scale factor. The increase of the scale a is equivalent to moving the frequency content of the mother wavelet towards lower frequencies. However, the decrease of a is equivalent to moving its frequency content towards higher frequencies. We opted for a scale factor δ = 0.005, giving a total of 380 frequencies. The time sampling and the number of points were, respectively, Δt = 0.005 s and N = 37,500.

The wavelet transform $WT\ (a,\tau)$ can be displayed on a 2D frequency versus time color plot, with the colors representing the magnitudes of $WT\ (a,\tau)$. Abrupt changes in the temporal signal affect the values of $WT\ (a,\tau)$ at all scales and can be easily detected. As our wavelet transform was complex-valued, it could be expressed in terms of the modulus $|\,WT\ (a,\tau)\,|$, which can be interpreted as the wavelet energy spectrum (i.e., scalogram). The magnitude of $WT\ (a,\tau)$ characterizes the occurrence and the intensity of the counterpart time scale at given time t. Consequently, the energy density of the signal $V_x\ (t)$ in the time scale plan could be estimated by:

$$E(a,\tau) = |WT\ (a,\tau)|^2 \tag{4}$$

Wavelet analysis offers a large choice in the form of mother wavelets to represent the temporal signal as compared to cosines and sines used in the Fast Fourier Transform (FFT) and Short-Time Fourier Transform (STFT). The wavelet-based energy of the Mexican hat [24], Daubechies [25], Shannon [26], and Morlet [20,21,27] mother wavelets for the time series of the velocity signal V_x resulting from the propagation of a JONSWAP (γ = 7) wave train (Case 120) are presented in Figure 5. The shapes of $E\ (a,\tau)$ were qualitatively similar when using different mother wavelets. Compared to the Morlet wavelet, more irregularities in $E\ (a,\tau)$ based on the Mexican hat, Daubechies, and Shannon mother wavelets were found, and smoothing operations may be needed to investigate frequencies present in the wavelet spectrum. Consequently, the Morlet mother wavelet was selected to be the most suitable for our purpose. The complex Morlet wavelet, also called the Gabor wavelet, can be interpreted as a sine wave tapered by a Gaussian window:

$$\psi(t) = \frac{1}{\sqrt{\pi \nu_0}} e^{-\frac{t^2}{\nu_0}} e^{j2\pi\omega_0 t} \tag{5}$$

where ν_0 is the bandwidth and ω_0 is the center frequency. A wider Morlet provides a weak temporal precision but good spectral precision, and vice versa for a narrower Morlet [28]. Obviously, the wavelet energy of the signal in the time scale plan was calculated for wavelets with different center frequencies ω_0 (namely 1, 1.5, 2, 2.5, 3, 3.5, 4, 4.5, 5, 5.5, and 6). For the signal decomposition, the maximum of the wavelet energy was used as an indicator for selecting the optimal center frequency ω_0 [29]. When ω_0 = 3 for most of the studied wave signals, the maximum of energy was obtained. Thus, the number three is the optimum frequency of the mother wavelet for signal decomposition. Concerning the bandwidth ν_0, it was fixed to 1 for real-time requirement and simplicity.

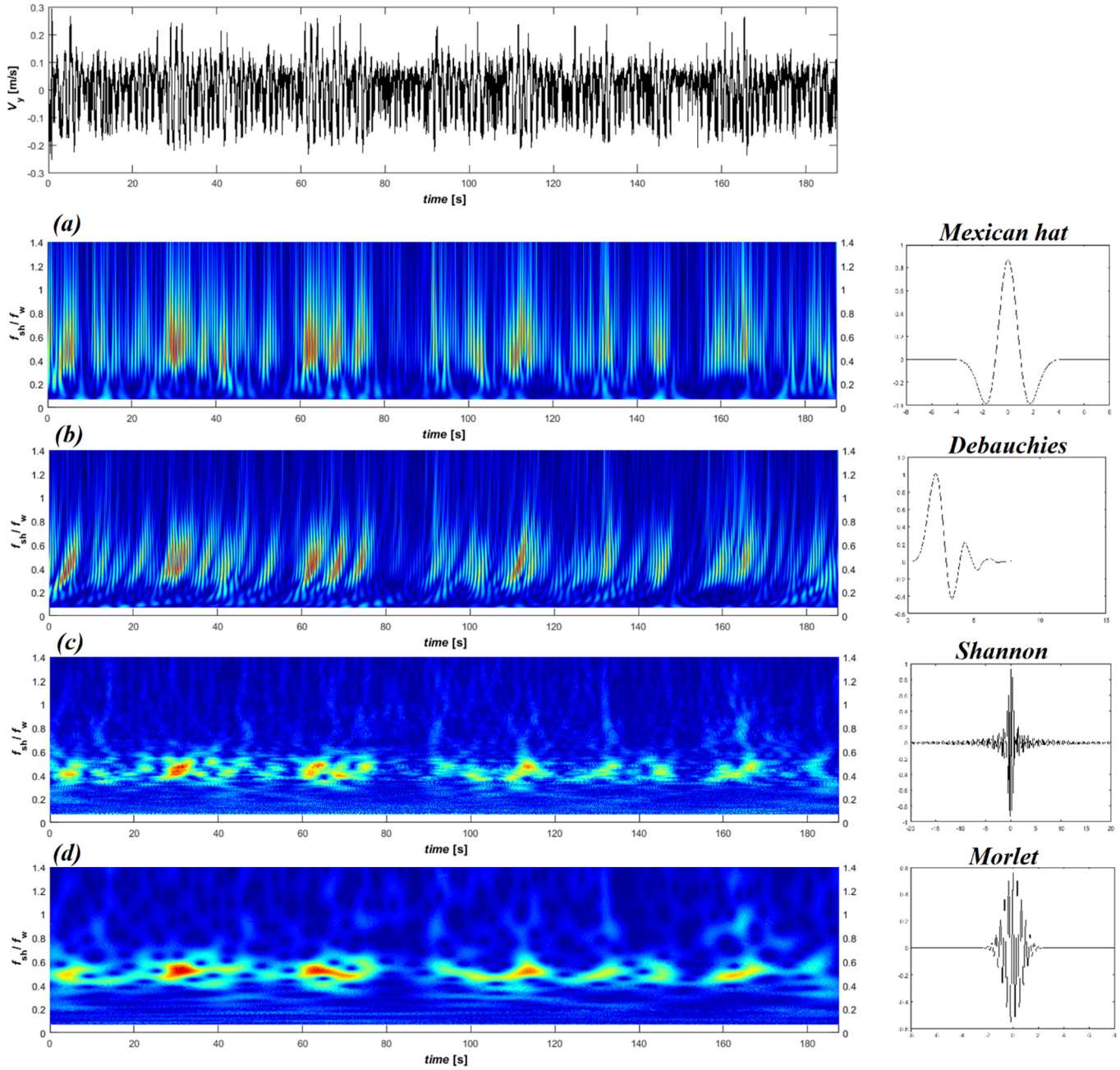

Figure 5. The velocity temporal evolution in the presence of a JONSWAP (γ = 7) wave train (Case 120), its wavelet-based energy $E(\tau,a)$ based on the (**a**) Mexican hat mother wavelet, (**b**) Daubechies mother wavelet, (**c**) Shannon mother wavelet, and (**d**) Morlet mother wavelet. The color bar indicates the wavelet energy.

Additionally, it can be useful to plot local maxima in the two-dimensional representation of wavelet information. These maxima, also called wavelet ridges, represent those locations in the time-frequency plan and are useful for pinpointing important frequencies at a given time t [21,28]. In addition to the energy wavelet density $E(a,\tau)$, to simplify its visualization, the dynamics of the local maxima (i.e., the time evolution of the wavelet ridges) can be calculated as follows:

$$\frac{\partial E(a,\tau)}{\partial a} = 0 \quad (6)$$

Figure 6 exhibits a simple illustration of the wavelet-based spectrum of the longitudinal velocity V_x in the presence of a sine wave with a frequency f = 1.35 Hz. Hans et al. [7] demonstrated that this wave belongs to the subharmonic lock-in region. Figure 6b shows a noticeable energetic band centered at f_{sh}/f_w = 0.5, which means that the subharmonic lock-in was continuously present. Figure 6c shows that the associated wavelet ridges were almost constant, i.e., dE~0, and deviated marginally from 0.5 to 0.5 ± 0.01 during the sinusoidal wave propagation. In other words, the effect of this sinusoidal wave on the vortex street led to the appearance of oscillations in the wake with a peak at half the frequency $f_w/2$, and a finite width of the wavelet spectral peak. For that reason, it was necessary to use a criterion by which one could determine if the subharmonic frequency lock-in occurred or not. As a criterion, we chose the width of the wavelet spectral peak. Only if the width of the wavelet spectral peak was less than 5% of f_{sh}/f_w = 0.5, this regime was defined as a subharmonic frequency lock-in.

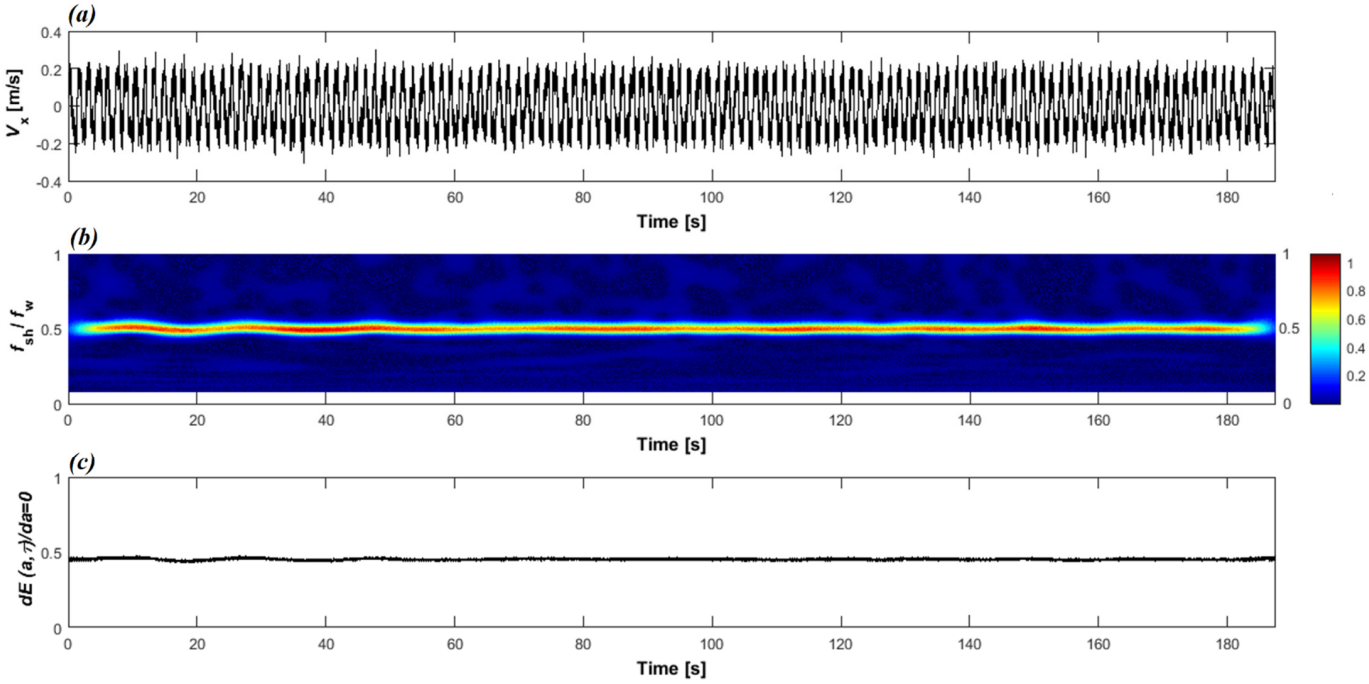

Figure 6. (**a**) The temporal evolution of the velocity V_x in the presence of a sine wave with frequency f = 1.35 Hz; (**b**) Temporal evolution of the wavelet spectrum energy E (a,τ); (**c**) temporal evolution of the wavelet ridges (presence of frequency lock-in). The color bar indicates the wavelet energy.

Generally, Figures 7–12 show that the complex Morlet power spectrum was found to highlight distinctive signatures in the presence and in the absence of the subharmonic frequency lock-in phenomenon. Figures 7–9 show the time series of the ADV of three wave trains in the presence of subharmonic synchronization, their wavelet energy E (a,τ), and their associated temporal evolution of the wavelet ridges. The respective patterns and graphs looked very similar. The first notable signature in the wavelet pattern was a strip of the domains aligned near f_{sh}/f_w = 0.5. This strip was formed by six domains that were red-yellow-shaded, and corresponded well to the trace path of the wave train.

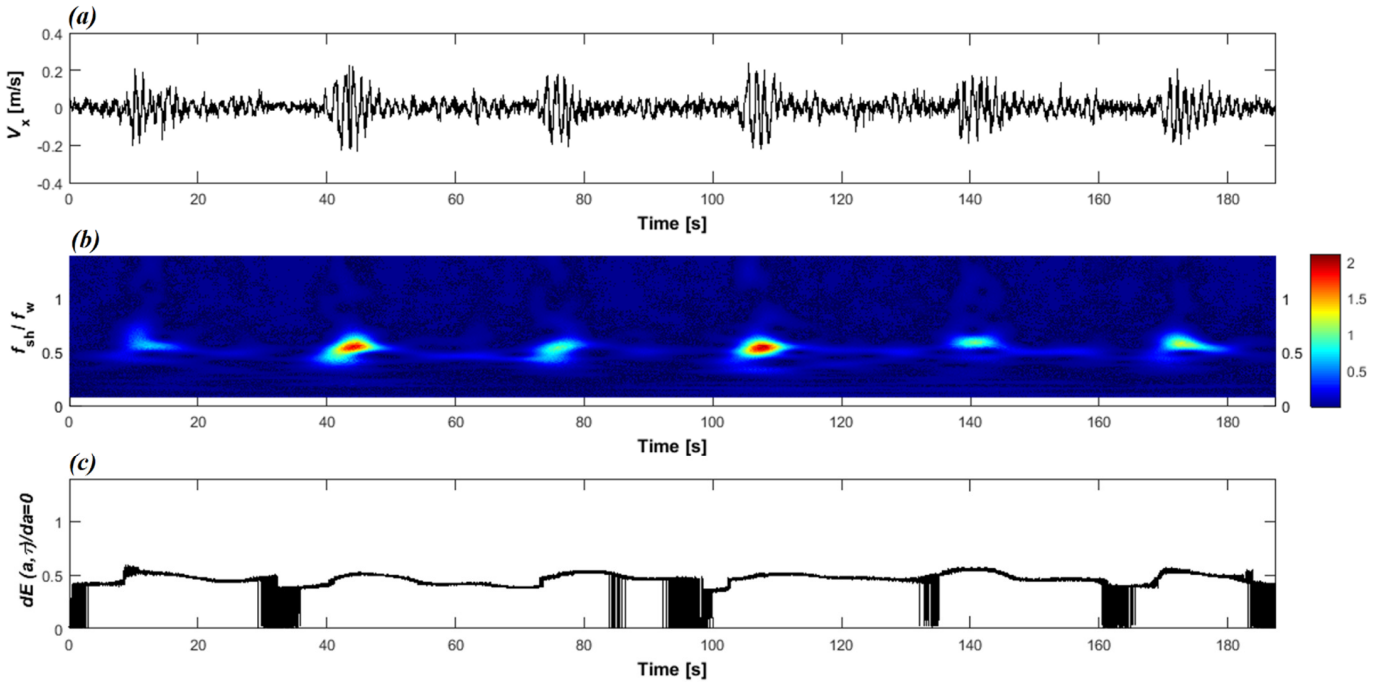

Figure 7. (**a**) The temporal evolution of the velocity V_x in the presence of a Pierson–Moskowitz wave train (Case 35), (**b**) temporal evolution of the wavelet spectrum energy E (a,τ), (**c**) temporal evolution of the wavelet ridges (presence of frequency lock-in). The color bar indicates the wavelet energy.

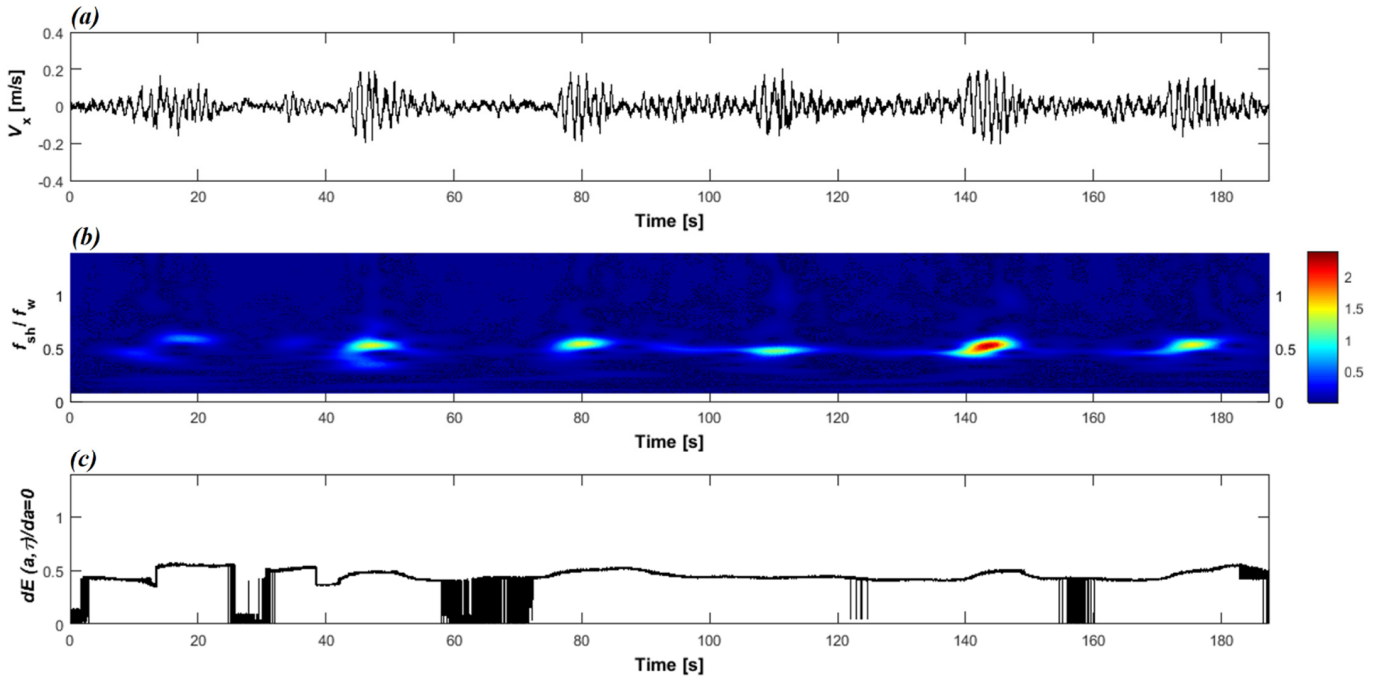

Figure 8. (**a**) The temporal evolution of the velocity V_x in the presence of a JONSWAP (γ = 3.3) wave train (Case 72), (**b**) temporal evolution of the wavelet spectrum energy E (a,τ), (**c**) temporal evolution of the wavelet ridges (presence of frequency lock-in). The color bar indicates the wavelet energy.

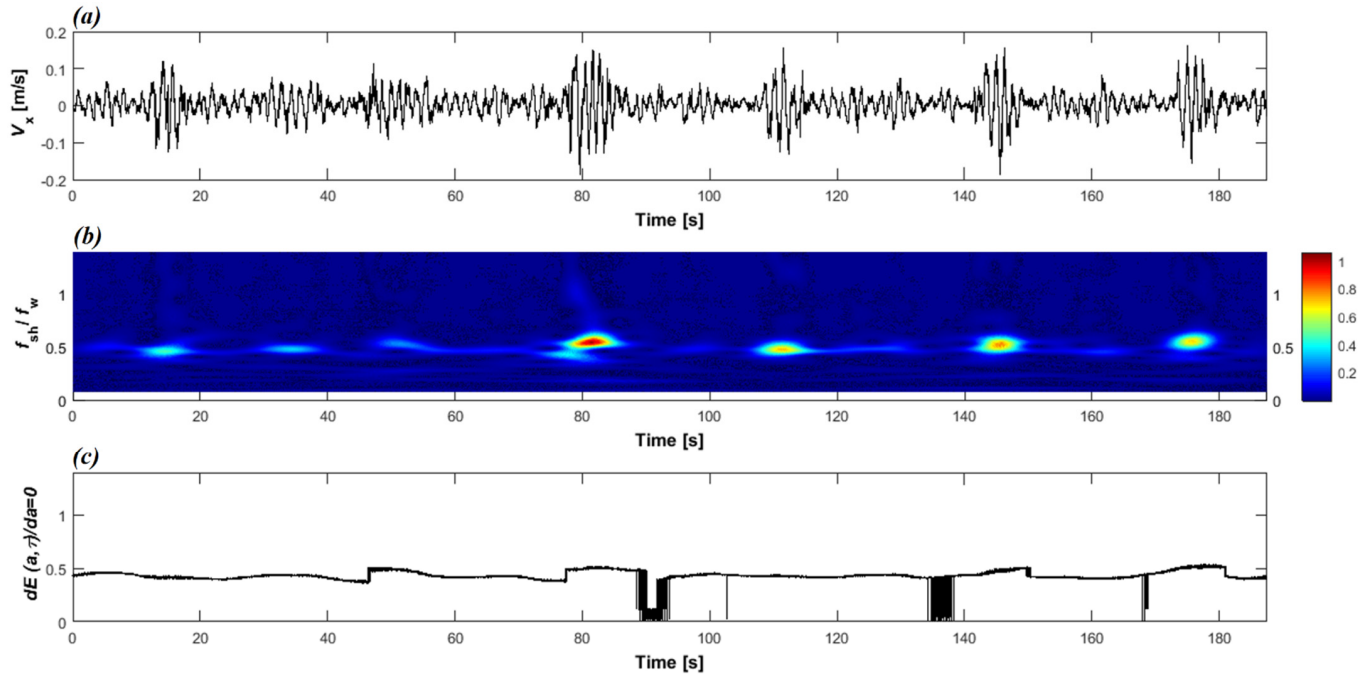

Figure 9. (**a**) The temporal evolution of the velocity V_x in the presence of a JONSWAP ($\gamma = 7$) wave train (Case 111), (**b**) temporal evolution of the wavelet spectrum energy E (a,τ), (**c**) temporal evolution of the wavelet ridges (presence of frequency lock-in).

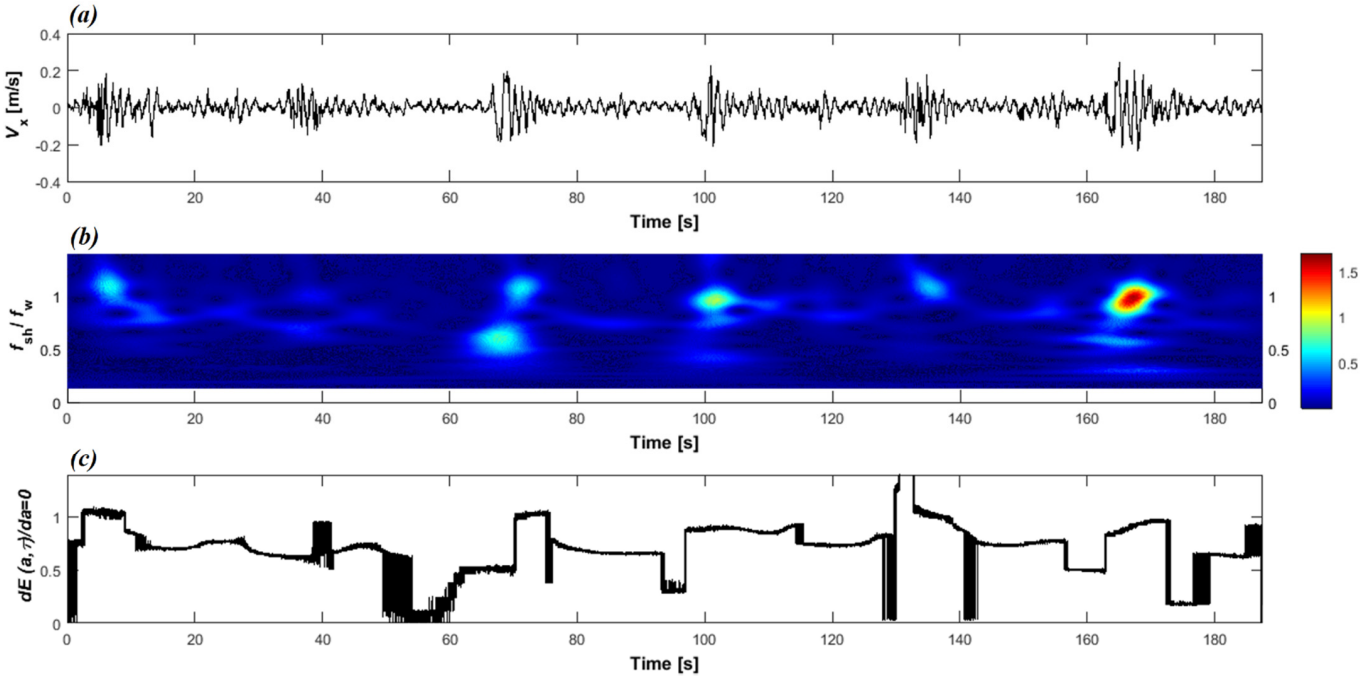

Figure 10. (**a**) The temporal evolution of the velocity V_x in the presence of a Pierson–Moskowitz wave train (Case 2), (**b**) temporal evolution of the wavelet spectrum energy E (a,τ), (**c**) temporal evolution of the wavelet ridges (absence of frequency lock-in). The color bar indicates the wavelet energy.

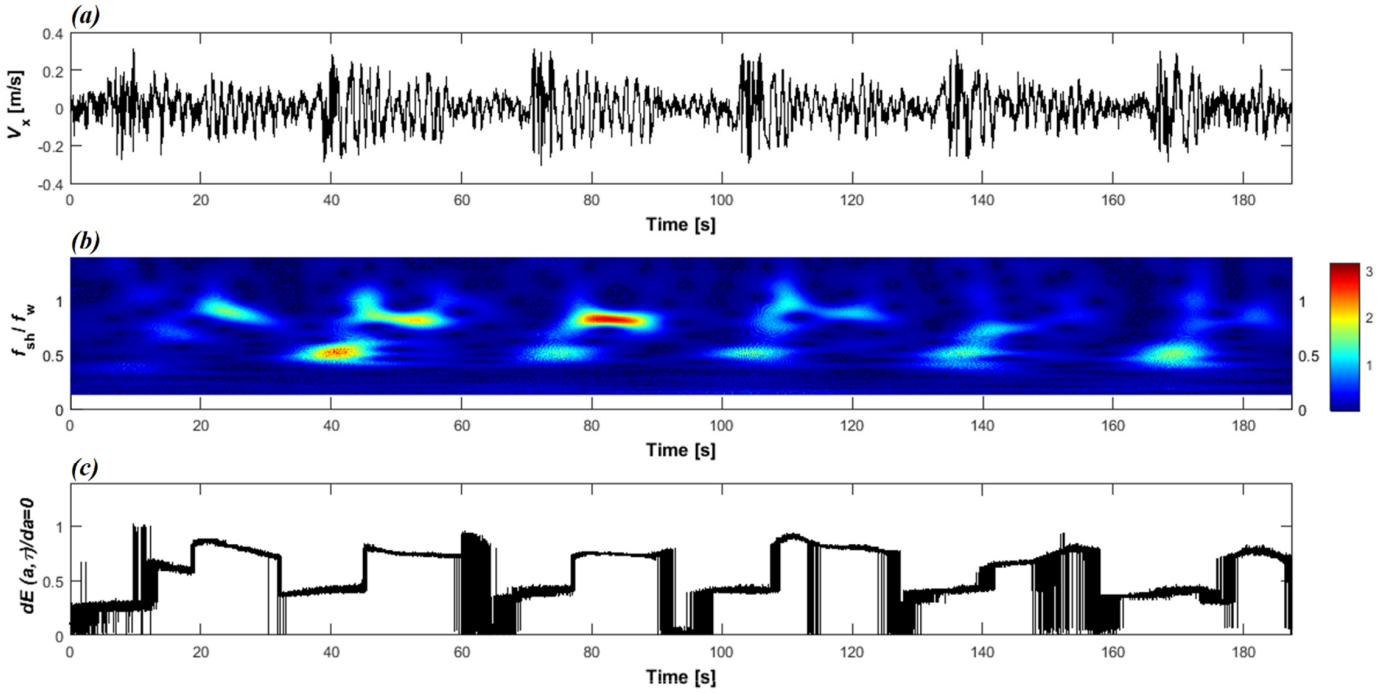

Figure 11. (**a**) The temporal evolution of the velocity V_x in the presence of a JONSWAP (γ = 3.3) wave train (Case 46), (**b**) temporal evolution of the wavelet spectrum energy E (a,τ), (**c**) temporal evolution of the wavelet ridges (absence of frequency lock-in). The color bar indicates the wavelet energy.

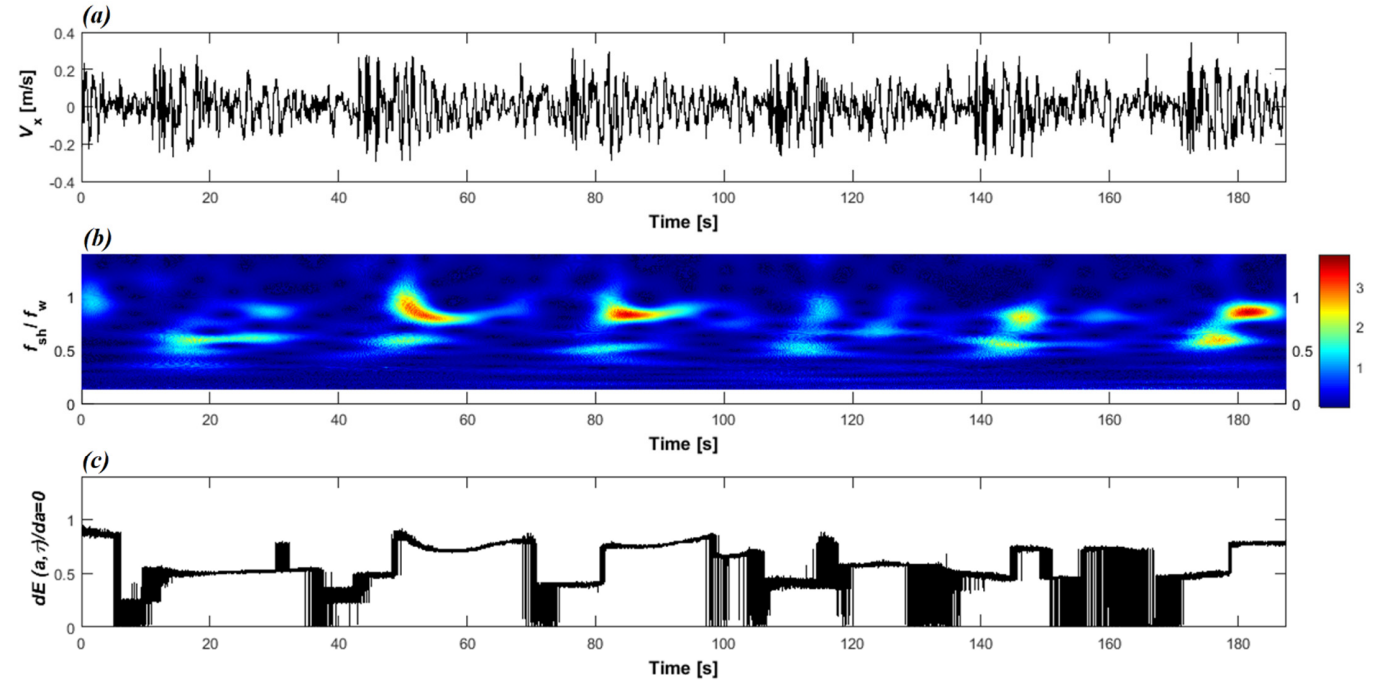

Figure 12. (**a**) The temporal evolution of the velocity V_x in the presence of a JONSWAP (γ = 7) wave train (Case 90), (**b**) temporal evolution of the wavelet spectrum energy E (a,τ), (**c**) temporal evolution of the wavelet ridges (absence of frequency lock-in). The color bar indicates the wavelet energy.

The second feature of the wavelet pattern was a large blue-colored domain, which could be distinguished above and under the red-yellow-shaded domains. These large blue domains indicated that the implication of frequencies $f < 0.45\, f_w$ and $f > 0.55\, f_w$ was less important. This means that the energy was mainly concentrated on the map zone, in which the frequency was $0.45\, f_w \leq f \leq 0.55\, f_w$. The third feature of the wavelet pattern

seen in Figures 7–9 was a narrower strip of the aligned domains near $f_{sh}/f_w = 0.5$ in the case of narrower wave train spectra. In other words, this strip was narrower in the case of a JONSWAP ($\gamma = 7$) wave train when compared to that of a Pierson–Moskowitz wave train. Thus, the wave train spectrum could be a reason why the strip of the domains near $f_{sh}/f_w = 0.5$ was narrow or wide. Moreover, wavelet ridges plots illustrated the presence of several zero slope regions following the passage of the wave train. Consequently, we could distinguish easily the duration of the subharmonic frequency lock-in phenomenon using wavelet ridges plots. It was also noted that in the case of narrow wave train spectra compared to wide wave train spectra, the wavelet ridges' temporal evolution contained less irregularities.

Figures 10–12 show the time series of the ADV of three wave trains in the absence of subharmonic synchronization, their wavelet energy $E(a,\tau)$, and their wavelet ridges' temporal evolution. The respective patterns and graphs in the absence of subharmonic synchronization looked very similar. The existence of a wide strip of red-yellow-colored domains allowed us to assume the existence of several implicated frequencies $0.2f_w \leq f \leq 1.5f_w$. Over time, additional several frequencies were involved in the wake of the cylinder, and chaotic frequency components appeared. In the absence of subharmonic synchronization, the shedding frequency was irregular in space, and vortex shedding did not occur periodically in time. The temporal evolution of the wavelet ridges demonstrated that local maxima varied randomly between 0 and 1.5 over time.

4. Conclusions

This paper discusses an experimental study of vortex shedding behind an elastically mounted cylinder in a water flow and in the presence of random wave trains propagating upstream. In the experiments, wave trains were generated via dispersive focusing technique in a two-dimensional wave flume. We investigated one hundred and twenty wave trains derived from Pierson–Moskowitz and JONSWAP ($\gamma = 3.3$ or $\gamma = 7$) spectra propagating in intermediate water depth. The experimental conditions were selected based on the wave nonlinearity S_0, the water depth $k_w h_0$, and the spectrum type.

The velocity measurements downstream the cylinder were used to examine the shedding frequency. Spectral evolution of the longitudinal velocity V_x was examined first. The shedding frequency f_{sh} and the spectral bandwidth were investigated as the nonlinearity and the water depth increased. The spectral bandwidth of the longitudinal velocity V_x decreased when the water depth increased. For water depth $k_w h_0 > 2.04$, the spectral peak reached $f_w/2$, and more than 90% of the spectral energy was inside the range $0.45 < f_{sh}/f_w < 0.55$. Hence, we could conclude the presence of a synchronization-like regime for water depth $k_w h_0 > 2.04$.

The Fourier transform has the assumption of a stationary signal, which means that features of the signal remain constant over time. However, nonstationarities are very important in the case of abrupt changes associated with extreme waves. The assessment over time of the variation of the shedding frequency behind the cylinder assists in easily identifying the subharmonic lock-in and its source. In order to accurately characterize the modes arising in the wake, the wavelet spectrum of the longitudinal velocity V_x was studied. Morlet wavelet was chosen as a mother wavelet given its large similarity with the ADV temporal signals.

From the experimental results, it was found that the wavelet energy and the associated ridges of the sampled data could clearly and precisely display locations of each singularity. In the presence of the subharmonic synchronization regime, the dominant frequency components lied in the range $0.45\, f_w < f_{sh} < 0.55\, f_w$.

Here, the wavelet technique was proven to be useful in identifying the frequency components of a physical system and its multiscale dynamics controlled by a nonstationary behaviour related to the extreme events. In similar contexts, Turki et al. [30,31] have used the spectral wavelet analysis to investigate the dynamics of storms from intermonthly to interannual scales. They found that the extreme energy spectrum at short scales should

be largely modulated to increase its impact at larger scales. It will be interesting to test the wavelet technique and the criterion by which one could determine if the subharmonic frequency lock-in occurs or not in the presence of rogue waves in field measurements. This could be achieved using the control procedure employed by [32] to record rogue wave signals and in the presence of a circular cylinder. A full investigation of this multi-timescale dynamics needs a coupling between different approaches of physical (use of experiments in laboratory), numerical (use of mathematical models), and stochastic (use of spectral techniques) which can be an important step to improve our understanding the extreme dynamics in coastal zones. It would also be interesting to investigate these findings in the presence of the cavitation phenomenon [33,34].

This study strengthens the utility of spectral approaches in detecting features that stay hidden in a classical Fourier analysis. Nevertheless, in order to expand results found in this study, efforts should be made by investigating shallower water conditions and higher nonlinearities with the presence of breaking. Finally, an inherent disadvantage of the dispersive focusing mechanism is scaling the results to full scale. Therefore, it will be interesting to compare our findings to field measurements.

Author Contributions: Conceptualization, I.A.; methodology, I.A.; formal analysis, I.A.; investigation, I.A.; resources, I.A. and F.M.; data curation, I.A.; writing—original draft preparation, I.A.; writing—review and editing, I.A., E.O., E.T. and N.A.; visualization, I.A.; supervision, N.A.; project administration, N.A.; funding acquisition, N.A. All authors have read and agreed to the published version of the manuscript.

Funding: This research was funded by the Normandy Region.

Institutional Review Board Statement: This study did not require ethical approval.

Informed Consent Statement: Not applicable.

Data Availability Statement: The free surface elevation and the ADV files of the one hundred and twenty wave trains used in this work are available in the supplement.

Acknowledgments: This work was carried out as part of the "DIAgnostique et Disponibilité des installations de production d'Energie électrique à partir des énergies MARines renouvelables" (DIADEMAR) project. The authors would like to acknowledge the Normandy Region for their financial support and to thank the M2C laboratory for the research facilities.

Conflicts of Interest: The authors declare no conflict of interest.

References

1. Jungsoo, S.; Yang, J.; Stern, F. The effect of air-water interface on the vortex shedding from a vertical circular cylinder. *J. Fluid Struct.* **2011**, *27*, 1–22. [CrossRef]
2. Williamson, C.H.K. Vortex dynamics in the cylinder wake. *Annu. Rev. Fluid Mech.* **1996**, *28*, 477–539. [CrossRef]
3. Olsen, J.F.; Rajagopalan, S. Vortex shedding behind modified circular cylinders. *J. Wind Eng. Ind. Aerod.* **2000**, *86*, 55–63. [CrossRef]
4. Hildebrandt, A.; Sriram, V. Pressure Distribution and Vortex Shedding Around a Cylinder due to a Steep Wave at the Onset of Breaking from Physical and Numerical Modeling. In Proceedings of the Twenty-Fourth International Ocean and Polar Engineering Conference, Busan, Korea, 15–20 June 2014.
5. Konstantinidis, E.; Balabani, S.; Yianneskis, M. Bimodal vortex shedding in a perturbed cylinder wake. *Phys. Fluids* **2007**, *19*, 011701. [CrossRef]
6. Lam, K.M. Vortex shedding flow behind a slowly rotating circular cylinder. *J. Fluid Struct.* **2009**, *25*, 245–262. [CrossRef]
7. Hans, G.; Abcha, N.; Ezersky, A. Frequency lock-in and phase synchronization of vortex shedding behind circular cylinder due to surface waves. *Phys. Lett. A* **2016**, *380*, 863–868. [CrossRef]
8. Kharif, C.; Pelinovsky, E. Physical mechanisms of the rogue wave phenomenon. *Eur. J. Mech. B-Fluid* **2003**, *22*, 603–635. [CrossRef]
9. Kharif, C.; Pelinovsky, E.; Slunayev, A. *Rogue Waves in the Ocean: Observations, Theories and Modelling*; Springer: New York, NY, USA, 2009; Volume 255. [CrossRef]
10. Fedele, F.; Herterich, J.; Tayfun, A.; Dias, F. Large nearshore storm waves off the Irish coast. *Sci. Rep.* **2019**, *9*, 15406. [CrossRef] [PubMed]
11. Vyzikas, T.; Stagonas, D.; Buldakov, E.; Greaves, D. The evolution of free and bound waves during dispersive focusing in a numerical and physical flume. *Coast. Eng.* **2018**, *132*, 95–109. [CrossRef]

12. Xu, G.; Hao, H.; Ma, Q. An experimental study of focusing wave generation with improved wave amplitude spectra. *Water* **2019**, *11*, 2521. [CrossRef]
13. Abroug, I.; Abcha, N.; Dutykh, D.; Jarno, A.; Marin, F. Experimental and numerical study of the propagation of focused wave groups in the nearshore zone. *Phys. Lett. A* **2020**, *6*, 126144. [CrossRef]
14. Tromans, P.S.; Anaturk, A.R.; Hagemeijer, P. A new model for the kinematics of large ocean waves-application as a design wave. In Proceedings of the First International Offshore and Polar Engineering Conference, Edinburgh, UK, 11–16 August 1991.
15. Milligen, B.P.V.; Sanchez, E.; Estrada, T.; Hidalgo, C.; Branas, B.; Carrersa, B.; Garcia, L. Wavelet bicoherence: A new turbulence analysis tool. *Phys. Plasma* **1995**, *2*, 3017–3032. [CrossRef]
16. Bai, Y.; Xia, X.; Li, X.; Wang, Y.; Yang, Y.; Liu, Y.; Liang, Z.; He, J. Spinal cord stimulation modulates frontal delta and gamma in patients of minimally consciousness state. *Neuroscience* **2017**, *346*, 247–254. [CrossRef]
17. Grinsted, A.; Moore, J.C.; Jevrejeva, S. Application of the cross wavelet transform and wavelet coherence to geophysical time series. *Nonlinear Proc. Geoph.* **2004**, *11*, 561–566. [CrossRef]
18. Young, I.R.; Eldeberky, Y. Observations of triad coupling of finite depth wind waves. *Coast. Eng.* **1998**, *33*, 137–154. [CrossRef]
19. Becq-Girard, F.; Forget, P.; Benoit, M. Nonlinear propagation of unidirectional wave fields over varying topography. *Coast. Eng.* **1999**, *38*, 91–113. [CrossRef]
20. Abroug, I.; Abcha, N.; Jarno, A.; Marin, F. Laboratory study of non-linear wave-wave interactions of extreme focused waves in the nearshore zone. *Nat. Hazard Earth Syst.* **2020**, *20*, 3279–3291. [CrossRef]
21. Tiscareno, M.S.; Hedman, M.H. A review of Morlet wavelet analysis of radial profiles of Saturn's rings. *Philos. Trans. R. Soc. A* **2018**, *376*, 2126. [CrossRef]
22. Farge, M. Wavelet transforms and their applications to turbulence. *Ann. Rev. Fluid Mech.* **1992**, *24*, 395–457. [CrossRef]
23. Torrence, C.; Compo, G.P. A practical guide to wavelet analysis. *Bull. Am. Meteorol. Soc.* **1998**, *79*, 61–78. [CrossRef]
24. Shark, L.K.; Yu, C. Design of matched wavelets based on generalized Mexican_hat function. *Signal Process.* **2006**, *7*, 1469–1475. [CrossRef]
25. Daubechies, I. *Ten Lectures on Wavelets*; Springer: Philadelphia, PA, USA, 1992. [CrossRef]
26. Ortiz-Gracia, L.; Oosterlee, A. A highly efficient Shannon wavelet inverse Fourier technique for pricing european options. *AIP Conf. Proc.* **2016**, *38*, 118–143. [CrossRef]
27. Turki, I.; Massei, N.; Laignel, B. Linking sea level dynamic and exceptional events to large-scale atmospheric circulation variability: Case of Seine Bay, France. *Oceanologia* **2019**, *61*, 321–330. [CrossRef]
28. Addison, P.S.; Watson, J.N.; Feng, T. Low-oscillation complex wavelets. *J. Sound Vib.* **2002**, *254*, 733–762. [CrossRef]
29. Feng, X.; Yunfei, L.; Xiping, W.; Brian, K.B.; Lon, A.Y.; Robert, J.R. Evaluation internal condition of hardwood logs based on AR-minimum entropy deconvolution combined with wavelet based spectral kurtosis approach. *Holzforschung* **2021**, *75*, 237–249. [CrossRef]
30. Turki, I.; Massei, N.; Laignel, B. Effects of global climate oscillations on Intermonthly to interannual variability of sea levels along the English channel coasts (NW France). *Oceanologia* **2020**, *62*, 226–242. [CrossRef]
31. Turki, I.; Baulon, L.; Massei, N.; Laignel, B.; Costa, S.; Fournier, M.; Maquaire, O. A nonstationary analysis for investigating the multiscale variability of extreme surges: Case of the English Channel coasts. *Nat. Hazard Earth Syst.* **2020**, *20*, 3225–3243. [CrossRef]
32. Christou, M.; Ewans, K. Field Measurements of rogue water waves. *J. Phys. Oceanogr.* **2014**, *44*, 2317–2335. [CrossRef]
33. Kolahan, A.; Roohi, E.; Pendar, M.R. Wavelet analysis and frequency spectrum of cloud cavitation around a sphere. *Ocean Eng.* **2019**, *182*, 235–247. [CrossRef]
34. Pendar, M.R.; Roohi, E. Cavitation characteristics around a sphere: An LES investigation. *Int. J. Multiph. Flow* **2018**, *98*, 1–23. [CrossRef]